Observing Grain Boundaries in CVD-Grown Monolayer Transition Metal Dichalcogenides

Thuc Hue Ly,[†,‡] Ming-Hui Chiu,[§] Ming-Yang Li,[⊥] Jiong Zhao,[†] David J. Perello,[†] Magdalena Ola Cichocka,[†,‡] Hye Min Oh,[†,‡] Sang Hoon Chae,[†,‡] Hye Yun Jeong,[†] Fei Yao,[†] Lain-Jong Li,[§] and Young Hee Lee[*,†,‡]

[†]IBS Center for Integrated Nanostructure Physics, Institute for Basic Science, Sungkyunkwan University, Suwon 440-746, Korea, [‡]Department of Energy Science, Department of Physics, Sungkyunkwan University, Suwon 440-746, Korea, [§]Physical Sciences and Engineering, King Abdullah University of Science and Technology, Thuwal 23955-6900, Saudi Arabia, and [⊥]Institute of Atomic and Molecular Sciences, Academia Sinica, Taipei 10617, Taiwan

ABSTRACT Two-dimensional monolayer transition metal dichalcogenides (TMdCs), driven by graphene science, revisit optical and electronic properties, which are markedly different from bulk characteristics. These properties are easily modified due to accessibility of all the atoms viable to ambient gases, and therefore, there is no guarantee that impurities and defects such as vacancies, grain boundaries, and wrinkles behave as those of ideal bulk. On the other hand, this could be advantageous in engineering such defects. Here, we report a method of observing grain boundary distribution of monolayer TMdCs by a selective oxidation. This was implemented by exposing directly the TMdC layer grown on sapphire without transfer to ultraviolet light irradiation under moisture-rich conditions. The generated oxygen and hydroxyl radicals selectively functionalized defective grain boundaries in TMdCs to provoke morphological changes at the boundary, where the grain boundary distribution was observed by atomic force microscopy and scanning electron microscopy. This paves the way toward the investigation of transport properties engineered by defects and grain boundaries.
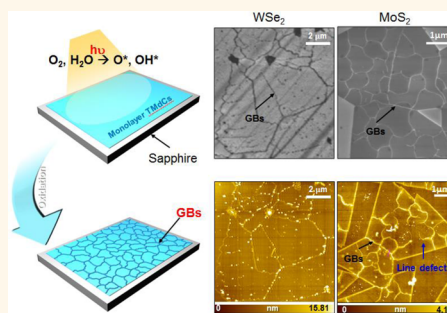
KEYWORDS: transition metal dichalcogenides · sapphire grain boundary · selective oxidation · atomic force microscopy · scanning electron microscopy · TEM · STEM

Grain boundaries in two-dimensional layered structure have attracted considerable attention from basic science and technology point of view.[1−5] Observing and engineering grain boundaries have been the key issues in controlling the grain sizes, their electronic properties, and the related device performances.[5−9] Grain boundaries and defects in graphene have been extensively studied not only at atomic scale using transmission electron microscopy and scanning tunneling microscopy,[1,10] but also at macro-scale with optical microscopy.[4,11,12] Unlike grain boundaries in graphene, less is known for grain boundaries in transition metal dichalcogenides (TMdCs).[3,5,13−16] The observation of grain boundaries of MoS$_2$ by second harmonic generation is a noninvasive and all optical way.[16,17] Yet, this method is not easily accessible, and thus, a simple and low cost approach to observe large-scale grain distribution is required if possible. Observation of grain boundaries in large-area monolayer TMdCs, for example, prepared by chemical vapor deposition (CVD), can provide a way of engineering the quality of grown TMdCs.

Our aim is to visualize grain boundaries (GBs) in large-area CVD-grown TMdCs. This approach is based on the oxidization of TMdC monolayer by UV irradiation at room temperature. O and OH radicals are generated by UV irradiation under moisture-rich conditions,[4,18] which subsequently oxidize defective grain boundaries. The width of GBs is narrow but can be widened by controlling UV oxidation conditions, in which such morphological modifications at the boundary can be observed by atomic force microscopy and scanning electron microscopy. This approach is not limited to metal or oxide substrate. This is well contrasted with previous reports on graphene grain boundaries where the oxidized metal below grain boundaries of graphene was observed.[4,11] The method is unique and

crucial for understanding GBs of a large family of CVD-grown transition metal dichalcogenides.

RESULTS AND DISCUSSION

To obtain information on grain boundary distribution in monolayer TMdC, large-area TMdC monolayer is convenient. Large-area monolayer WSe$_2$ (2×1 cm^2) was synthesized on sapphire by CVD, using WO$_3$ powder and Se powder as the precursors[19] (see Methods for details). The sample was used directly without transfer to minimize unwanted effects involved during transfer process. Large-area monolayer WSe$_2$ on sapphire substrate was loaded into a UV chamber at a humidity level of 65%. UV light irradiation generates O and OH radicals,[4] which can be easily bonded on the defects near the GBs and point defects.[4] A schematic for UV oxidation is shown in Figure 1a. In general, the width of GBs is expected to be as narrow as a nanometer and is not easily observed even with atomic force microscopy (AFM) and scanning electron microscopy (SEM) in a few micrometer sizes (Figure 1b,c). The brighter spots in AFM and darker spots in SEM are multilayer portions which were generated during CVD growth.[19] Monolayer WSe$_2$ on sapphire was uniformly synthesized without explicit voids in large area of 2×1 cm^2. No distinctive grain boundary lines were observed from a series of AFM and SEM images due to the limited resolution. The characteristics of large area monolayer WSe$_2$ has been described elsewhere.[19]

After the sample was irradiated by UV light for 6 min at room temperature under moisture-rich conditions, the grain boundary lines were visible as the bright lines in the morphological image of AFM (Figure 1d). The similar dark lines were also observed in SEM image at the identical position to AFM (Figure 1e). Since WSe$_2$ on sapphire substrate (Al$_2$O$_3$) was directly used, neither artifacts in bare sapphire substrate nor such morphological patterns were created to influence morphology (Supporting Information Figure S1). The morphological change in the AFM image was ascribed to the oxidation at the grain boundary of WSe$_2$ layer. This is well contrasted with UV oxidation of grain boundary in graphene where the underlying copper was oxidized to reveal morphological changes in optical microscopy.[4] Grain boundaries in WSe$_2$ layer might be defective and can be easily oxidized to reveal such morphological modifications under oxidation.

To understand how the GB lines are generated on WSe$_2$ layer, we prepared samples with different UV irradiation times. The humidity level was maintained at 65%. Lower humidity was not sufficient to generate GB lines. At low humidity level (less than 40%), GBs were observed at longer humidity time (10 min) (Supporting Information Figure S2), which is in good contrast with that at 65% that partial oxidation occurred (Figure 2a). Pure ozone treatment involved etching only but no GB lines were generated. The presence of moisture was very necessary to produce OH radicals under UV irradiation.[20−23] These radicals played an important role for being attached on GBs to oxidize WSe$_2$. At high humidity level (60−65%), observations of GBs in ($10 \times 10 \ \mu$m^2 WSe$_2$) relied on the UV treatment time clearly (Figure 2). White spots, regarded as oxidized point defects and impurities such as vacancies, higher
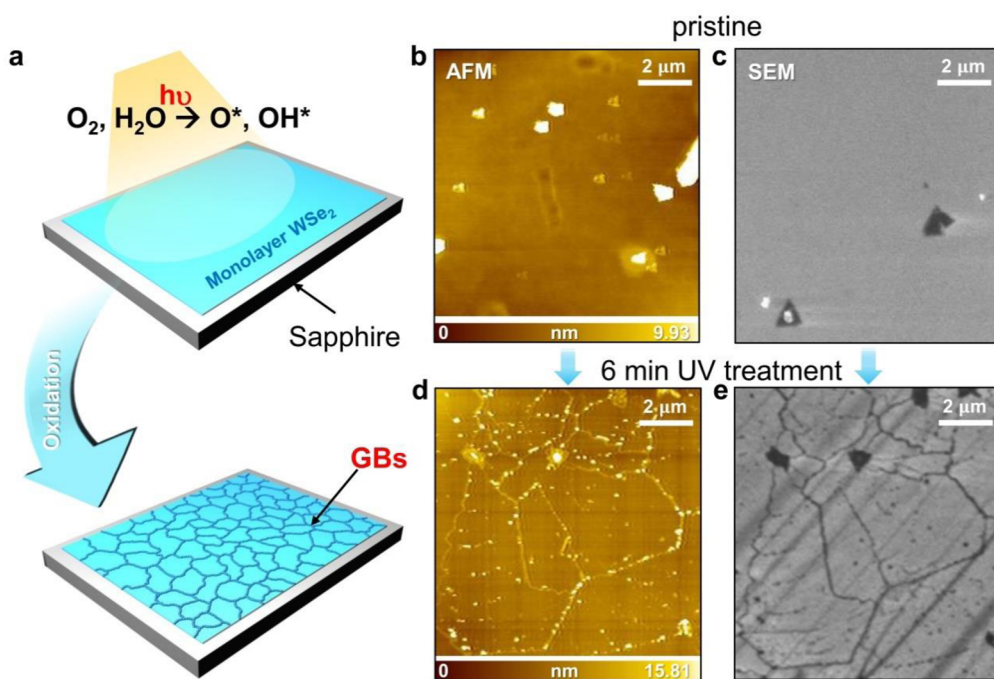

Figure 1. Schematic of the ultraviolet irradiation process. (a) Schematic diagram for UV treatment monolayer WSe$_2$. (b and c) AFM and SEM image of pristine WSe$_2$. (d and e) AFM and SEM image of oxidized WSe$_2$ after 6 min UV treatment.
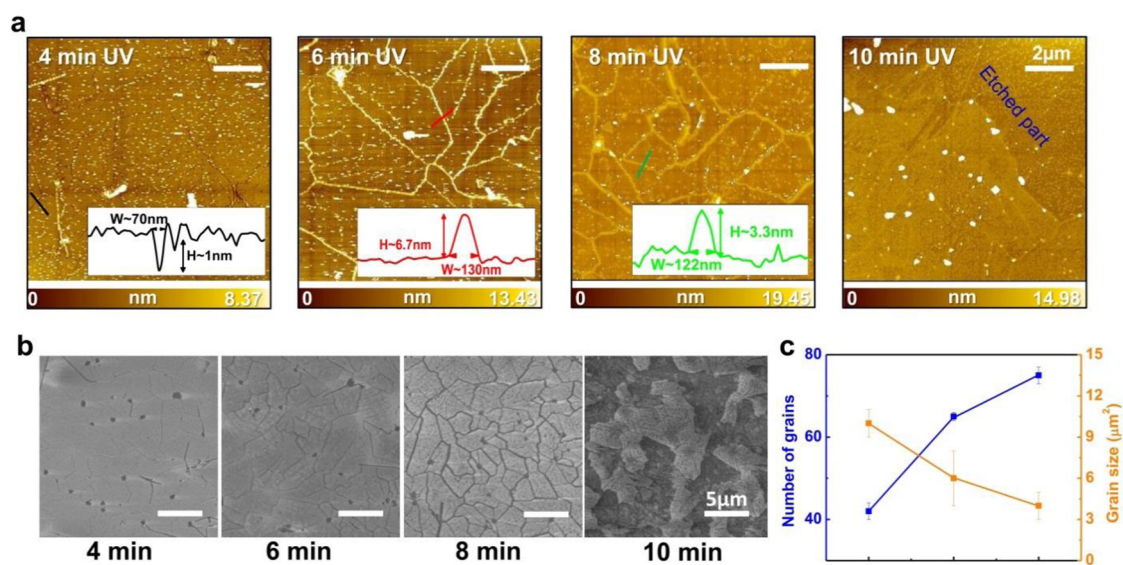
Figure 2. UV reaction time dependence of WSe$_2$ in ambient condition with humidity of ∼65%. (a) AFM images with 4, 6, 8, 10 min UV exposure time. Inserts are height profiles of lines. (b) SEM images with different UV treatment time. (c) Statistic of number of grains and grain size with 4, 6, 8 min UV treatment time.

order vacancies, and/or excessive seleniums, were scattered on the entire surface of WSe$_2$ layer and some GB lines partially appeared under 4 min UV oxidation (Figure 2a). The inset revealed a depth profile (not a height) of ∼1 nm with a width of ∼70 nm. Higher resolution image (Supporting Information Figure S3a, d) clearly demonstrated that GB lines are composed of oxidized parts with a height profile (white spots) and dark parts with a depth profile (trench parts). This strongly implies that some portion of grain boundaries oxidized in earlier stage was etched away to give a depth of ∼1 nm, similar to the thickness of monolayer WSe$_2$. Such an observed etching process on WSe$_2$ by UV oxidation is attributed to weak bonds in WSe$_2$, which is different from graphene that showed no such etching phenomena under similar conditions.[4] Further oxidation for 6 min led to accumulate functional groups to have thick boundary lines. Line profile which runs across the GBs showed a height of ∼6.7 nm and the line width was expanded to ∼130 nm (inset of 6 min UV). Optical micrograph also showed similar patterns in this case (Supporting Information Figure S4). Slightly different heights were observed from other positions (Supporting Information Figure S3e), indicating that nature of defects at the GB of WSe$_2$ layer is in fact complicated. The height of GBs was reduced to ∼3.3 nm at 8 min UV oxidation, again a partial etching behavior, as evidenced by the empty area near the middle of the image (circle), while the width did not change much. The GB lines were nearly saturated here with similar patterns to those of 6 min UV oxidation. At 10 min UV oxidation, some portions (upper right corner) were completely etched away. AFM observations indicate that 6 min UV oxidation is the best for observing grain boundaries in WSe$_2$ layer.

Similar phenomena were observed by SEM (Figure 2b) and optical microscopy (Supporting Information Figure S4). For example, at 2 min UV oxidation time, a few lines were developed with some etch pits (see also Supporting Information Figure S5). The rich white speckles appeared in AFM image were not visible in the same size of SEM image. Although some lines appeared at 6 min UV oxidation, more distinct grain boundary lines were observed at 8 min UV oxidation. Narrow grain boundary lines developed at 6 min oxidation time shown in AFM image were rarely visible in SEM image. WSe$_2$ layer was severely etched away at 10 min UV oxidation, similar to AFM observations. Images were not clear enough from optical microscopy due to relatively narrowly oxidized region (Supporting Information Figure S5), although similar trends to AFM and SEM observations were observed. Information for the average number of grains and average grain sizes by counting the number from different positions of the samples was extracted (Supporting Information Figure S4). The average number of grains increased with oxidation time and saturated at 8 min oxidation time, while the average grain sizes decreased with oxidation time (Figure 2c). We conclude that our UV oxidation approach can visualize intrinsic grain boundary distribution of monolayer WSe$_2$ at an optimum condition of 6 min UV oxidation under 65% humidity, not intentionally generated by creating defects on WSe$_2$ plane.

In addition to the morphological modification observed in AFM and SEM images, we also performed spectroscopic analysis using Raman spectroscopy and photoluminescence (PL) (Figure 3). The two characteristic peaks from Raman spectra for monolayer WSe$_2$ at 248.7 cm^{-1}, assigned to E$^1_{2g}$ mode, and 260 cm^{-1},
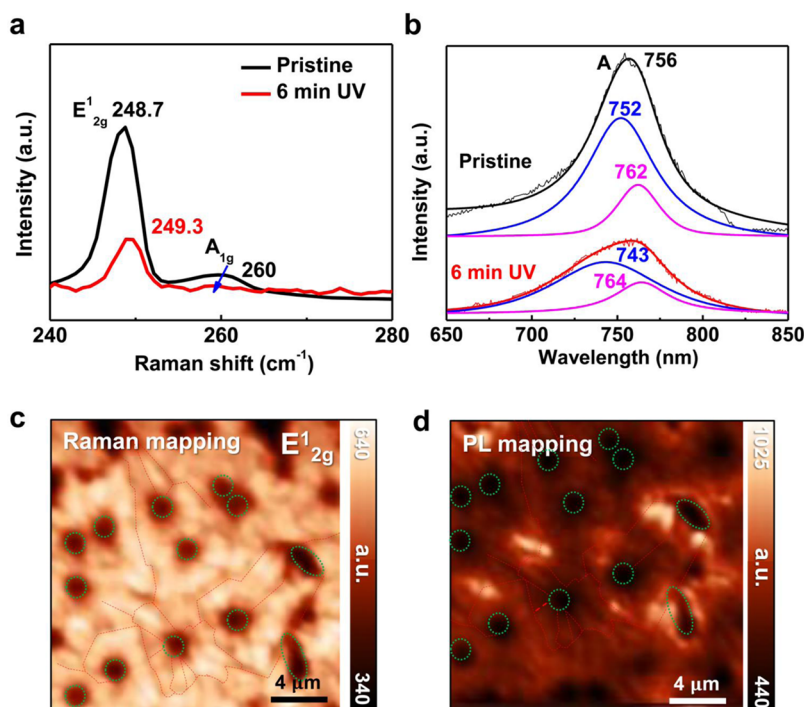
Figure 3. Monolayer WSe$_2$ exposed to UV light with a humidity level of ∼65% for 6 min. The data are collected from dark portions that are related to GBs for confocal Raman and PL mappings. (a) Raman and (b) PL spectra of the pristine and UV-treated samples. The black/red lines are the experimental data. The thin lines are the deconvoluted results with two curves (blue and magenta) using Lorentzian + Gauss peak fitting. (c) Confocal Raman and (d) PL mappings after UV treatment.

assigned to A$_{1g}$ mode, were observed.[19,24,25] After UV oxidation for 6 min, Raman and PL single spectra are taken from the darker positions for mapping image that are related to GB regions. The E$^1_{2g}$ peak was slightly upshifted to 249.3 cm^{-1} with significantly reduced intensity, and the intensity of A$_{1g}$ was also reduced after oxidation. The A exciton peak in PL spectra (excited by a 532 nm laser) of monolayer WSe$_2$ near ∼756 nm[19,26−28] revealed a significant intensity reduction after oxidation. B exciton was not observed in our case perhaps due to low laser power. One can notice that the line shape of PL spectra after oxidation is different from that of the pristine sample. To distinguish the peaks of PL spectrum, the curve was deconvoluted into two peaks by using mixed Lorentzian and Gauss curves, as shown in Figure 3b. The peak near 752 nm was blueshifted to 743 nm by oxidation, ascribed to the p-type doping effect due to oxidation.[29] Another peak near 762 nm was not shifted appreciably, which comes from nonoxidized portion. Confocal Raman mapping with an integration of E$^1_{2g}$ peak (240−254 cm^{-1}) is shown in Figure 3c. The GB lines were visible with dark regions, marked by red dotted lines. The circles indicate vortex point where several grains are merged. These are in fact well correlated with PL mapping, although the contrast from GB lines is not so obvious. Without UV treatment, no distinct corrugated line pattern was observed in both confocal Raman and confocal PL intensity mapping (Supporting Information Figure S6a,b). This was also observed in SEM image in Figure 1c.

GB lines and white spots (presumably multilayer portion) were observed in AFM (Supporting Information Figure S7a), in which some thick dashed lines are marked for guidance. Because of the large spot size of the laser (∼500 nm), grain boundary lines that are located closely to each other, were not distinguishable neither in confocal Raman nor confocal PL intensity mapping. Oxidation of the WSe$_2$ layer was further confirmed by X-ray photoelectron spectroscopy (XPS) of two samples (Supporting Information Figure S8).

Grain boundaries are presumably formed by simply stitching small flakes during growth. In such a case, the grain orientations in general differ from each other. To confirm what we observed as grain boundaries in WSe$_2$ layer is indeed the true grain boundaries, not artificially constructed defect lines, it is required to identify the different grain orientations separated by such observed lines. For this purpose, we performed TEM observations. After transfer of the monolayer WSe$_2$ on TEM grid, large-area WSe$_2$ layer seemed to be fragmented (Figure 4a). A similar phenomenon was also observed by optical microscopy when the sample was transferred to SiO$_2$/Si substrate (Supporting Information Figure S9). The grain boundaries could be mechanically weak[2,18] so that they could be ruptured during transfer process which often involves severe mechanical strain. The dark field image and the corresponding selective-area electron diffraction (SAED) pattern were obtained from the red circle region marked in Figure 4a which shares three regions in the corner.
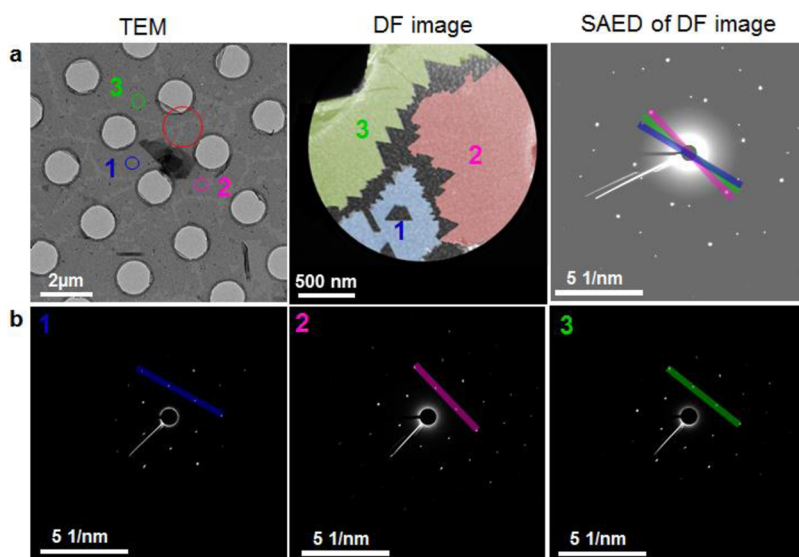
Figure 4. Grains in monolayer WSe₂. (a) TEM image of WSe$_2$ layer without oxidation on TEM grid, dark field image, and the corresponding selective-area electron diffraction (SAED) pattern were obtained from the red circle region marked in TEM image. Most of grain boundaries were cracked during transfer. (b) A series of SAED patterns marked by different small circles (1, 2, 3) in (a) clearly demonstrated different crystal orientations.

Three different colors were shown in the dark field image separated by the crack (region 1). Three different hexagonal spots with different intensities were visible in the SAED pattern. A series of SAED patterns marked by different small circles (1, 2, 3) clearly demonstrated different crystal orientations (Figure 4b). More examples of such orientation distribution from different regions were provided (Supporting Information Figures S10 and S11). Note that the grain size here is an order of a few micrometers, which is similar to those obtained from AFM image. Therefore, we conclude that the grain boundaries we observed by AFM are true grain boundaries separated by grains with different orientations. Monolayer WSe$_2$ layer is mechanically weak. In addition to the ruptured grain boundaries, the cracks were often visible within the grain that maintained the same crystal orientation (Supporting Information Figure S12), in good agreement with previous prediction.[2,3]

Grain boundaries are presumably formed during CVD growth. Nucleation of WSe$_2$ could be initiated randomly from impurities or defects on substrate. As the size of WSe$_2$ grows, they could merge and form grain boundaries. Size of grains depends on the number of nucleation seeds and CVD growth conditions. In addition to forming grain boundaries, points defect could be generated easily. There has been no report on such point defects on CVD-grown WSe$_2$ monolayer. The high-resolution TEM image was provided in Supporting Information Figure S13. The middle part of Figure 13a and its high-resolution TEM (Supporting Information Figure S13b) revealed highly crystalline WSe$_2$ layer. The contaminant shown in Supporting Information Figure S13a at the edge area contained amorphous carbon coming from the residual PMMA

and carbon TEM grid. Annular dark-field image—scanning transmission electron microscope (ADF-STEM) was also shown to see clearer image with high crystallinity in atomic scale (Supporting Information Figure S13c). The magnified TEM image for the area squared by green solid line in Supporting Information Figure S13c revealed the hexagonal lattice structure of WSe$_2$ (Supporting Information Figure S13d). The identified W and Se atoms provided their relative positions (d_{W-Se} = 2.58 Å, d_{W-W} = 3.25 Å), in good agreement with theoretical prediction of monolayer 2H-WSe$_2$ phase.[30] It is intriguing to see in other area that selenium vacancy (blue square and Supporting Information Figure S13f) and higher order defects exist (Supporting Information Figure S13e). The defect population became richer as the beam scan time persisted (Supporting Information Figure S14). Although low electron energy of 80 keV was used for STEM, the sample could be damaged to generate point defects due to weak mechanical strength of WSe$_2$ monolayer.[31−33] With longer scanning time, Se-vacancies were generated more but no W vacancies were observed. This is in good contrast with MoS$_2$ monolayer that Mo- and S-vacancies were observed with electron beam irradiation.[14]

Oxidation of the WSe$_2$ layer was further confirmed by energy-dispersive X-ray (EDX) quantitative analysis (Supporting Information Figure S15). The net increase of oxygen content after 6 min UV treatment was only ∼1.49% because the region of the oxidized WSe$_2$ was very narrow, located at the WSe$_2$ grain boundaries, in agreement with XPS observations in Supporting Information Figure S8. The ratio of W/Se was increased from 0.43 (before UV) to 1.01 (after UV treatment) due to the reduced Se content, indicating Se etching during
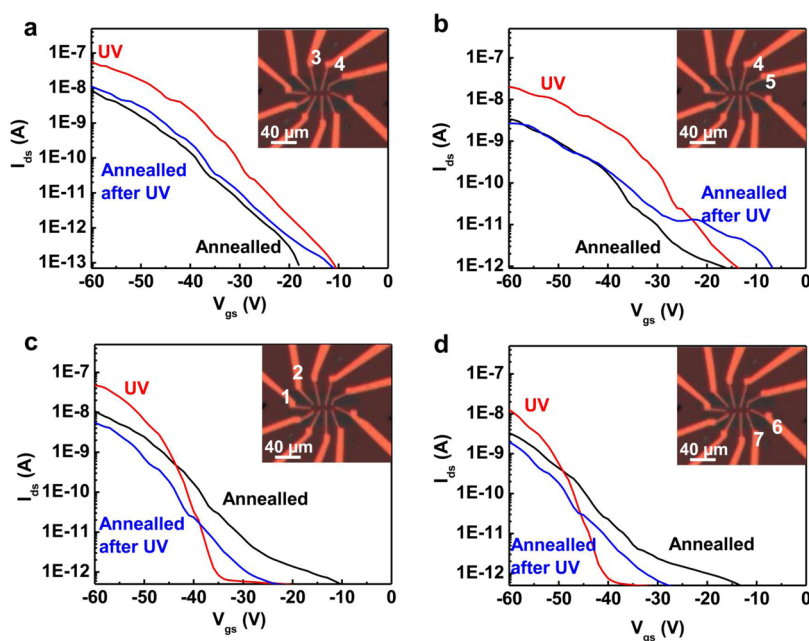
Figure 5. Transport measurement of monolayer WSe$_2$ with UV treatment. $V_{gs}-I_{sd}$ measurements were performed for a number of samples at three different conditions: after initial annealing at 150 °C for 1 h in vacuum, after UV treatment, and after reannealed again at 150 °C for an hour.

UV oxidation. The electron energy loss spectrum (EELS) of WSe$_2$ before and after UV treatment was also observed (Supporting Information Figure S16). The O K edge was detected only after UV treatment, in which such oxygen atoms formed amorphous WO$_{3\pm\delta}$, again indicating that the WSe$_2$ layer was oxidized after UV treatment.

The electrical measurement was carried out to provide useful information on oxidation of WSe$_2$ layer. A back-gated WSe$_2$ FET was fabricated on 300 nm SiO$_2$/Si substrate *via* standard electron beam lithography (see Methods for details). Transfer characteristics of devices were measured in μTorr vacuum for the sample after annealing, the UV-treated sample for 5 min, and the reannealed sample after UV treatment (Figure 5). Initial state of the sample after vacuum annealing showed p-FET behavior with low I_{on} of ~10 nA, resulting from negative threshold voltage (Figure 5a). After UV treatment, I_{on} was observed to increase 10-fold and the threshold voltage was slightly upshifted, consistent with a hole (p-) doping effect of oxygen generated under UV treatment. With reannealing of the UV-treated sample, the on-current was nearly recovered to its original value. The similar behavior was shown in another set of device (Figure 5b). On the other hand, Figure 5c,d shows another type of IV characteristics. With UV treatment, I_{on} increased similar to the previous cases. However, after reannealing, I_{on} was further reduced below the initial value and moreover, the threshold voltage was further shifted to negative value. We observed these two patterns of IV characteristics from other sets of devices. Simple physisorbed oxygen-related functional groups play a role in shifting the

on-current and the threshold voltage in the former case. Strong chemisorbed functional groups can be involved during UV process in the latter case, which modify further the TMD surface with reannealing. This requires further study.

The same argument can be applied to other TMdC materials. To generalize our approach, MoS$_2$ monolayer was tested further (Supporting Information Figure S17). Two MoS$_2$ flakes were merged together. After the similar oxidation process, the grain boundary line was observed in the merged region from AFM morphology, although additional oxidized line defects were visible. We note that oxidation occurred more easily in MoS$_2$ than WSe$_2$ such that extra oxidation occurred even within the grain from high resolution AFM image. Clear grain boundary distribution was observed exclusively from large-area MoS$_2$ monolayer in SEM image. The formation of line defects requires further study.

CONCLUSIONS

In conclusion, we demonstrated an easy method for observing grain boundaries and defects of large-area CVD-grown tungsten diselenide. This technique was realized by generating oxygen and hydroxyl radicals using UV irradiation under moisture-rich conditions and selectively functionalizing defective grain boundaries in WSe$_2$ to provoke morphological changes at the boundary. We observed both etching and oxidation occurred simultaneously at the grain boundary, which is more complicated than graphene. The atomic structure of WSe$_2$ and Se vacancy observation were reported for the first time to our knowledge.

Although the degree of oxidation is different from material to material, a similar oxidation approach can be used to investigate grain boundary distribution and point defects for the layered structures including TMDs.

METHODS

Growth of WSe₂ Full Film. The WO_3 powders (0.3 g) were put in a quartz boat and placed in the heating zone center of the furnace. The Se powders were prepared in a separate quartz boat at the upper stream side of the furnace. The sapphire substrates for growing WSe_2 were put at the downstream side, next to WO_3 powders quartz boat. The gas flow was brought by an Ar/H₂ flowing gas (Ar = 90 sccm, H₂ = 9 sccm), and the chamber pressure was controlled at 4 Torr. The center heating zone was heated to 925 °C at a ramping rate 28 °C/min, and the temperature of Se boat was maintained at 290 °C by heating tape during the reaction. Note that the temperature of the sapphire substrates was at about 850 °C when the center heating zone reaches 925 °C. After reaching 925 °C, the heating zone was kept for 15 min for reaction and the furnace was then naturally cooled down to room temperature.

Growth of MoS₂ Film. The MoO_3 powder (0.3 g) was placed in a ceramic boat located in the heating zone center of the furnace. The S powders were placed in a separate ceramic boat at the upper stream side maintained at 150 °C during the reaction. The sapphire substrate for growing MoS_2 was located at the downstream side, where the S and MoO_3 vapors were brought to the targeting sapphire substrate by an Ar carrier gas (70 sccm, chamber pressure = 40 Torr). The center heating zone was heated to 635 °C with a ramping rate 15 °C/min. After reaching 635 °C, the heating zone was kept for 30 min and the furnace was then naturally cooled down to room temperature.

Ultraviolet Oxidization of TMdCs on Sapphire. TMdCs grown on sapphire were placed into a chamber equipped with a low-pressure Hg lamp (LH-arc, Lichtzen, with an output of 20 mW cm^{-2}), with the majority of emitted light at a wavelength of 254 nm and approximately 10% of emitted light at a wavelength of 185 nm. Humidity was introduced into chamber by connecting it to a humidifier. The humidity level in the chamber was monitored using a hydro-thermometer (accuracy of $\pm 3\%$), where the chamber was continuously ventilated to maintain a constant pressure. After reaching the required humidity level, the humidifier was disconnected from the chamber. The TMDCs on sapphire was then irradiated under UV light for different times (2, 4, 6, 8, and 10 min). Radicals are generated under UV and humidity conditions as follows:

$$O_2 \rightarrow O_3$$

$$O_3 + H_2O \rightarrow O_2 + H_2O_2$$

$$2O_3 + H_2O_2 \rightarrow 2OH^* + 3O_2$$

$$H_2O \rightarrow H^* + OH^*$$
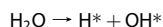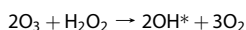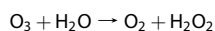
Device Fabrication. WSe₂ monolayer in a millimeter scale was transferred onto Si substrate with 300 nm SiO_2 using a wet etching method (will be described in TEM sample preparation below). Source/drain contacts were fabricated using e-beam lithography followed by metal evaporation of Ti/Au (7/30 nm) films. The channel was patterned with e-beam lithography again and the unwanted WSe₂ layer was removed using SF_6 plasma etching. The transport measurements were then performed with voltage probes (Keithley 4200) using a probe station with gold tip.

Characterization. The morphology of WSe₂ on sapphire was observed by optical microscopy (100× magnification, ZEISS, Axio Imager 2), field emission scanning electron microscopy (FESEM, JEOL JSM7000F, Japan), atomic force microscopy (SPA 400, SEIKO, Japan) in tapping mode. 2D confocal Raman mapping and PL mapping were also performed using NT-MDT, NTEGRA Spectra PNL (see Supporting Information, Experimental Methods for more details.). The crystal structure of WSe₂ on sapphire was analyzed with transmission electron microscope (TEM, JEM ARM 200F) and probe aberration-corrected scanning transmission electron microscope (STEM, JEM ARM 200F) operated at 80 kV under STEM mode.

TEM Sample Preparation. The sample was transferred to a quantifoil TEM grid with a gold supported thin film (PELCO, 200 mesh, gold, 1.2 μm holes), using a thin PMMA support. A thin layer of PMMA C4 (MicroChem, 4 wt % in chlorobenzene) was spun onto the WSe₂/sapphire (4000 rpm, 60 s, 2 times) without a postbaking step. The WSe₂ and PMMA support was then detached from sapphire by floating the WSe₂/sapphire, PMMA side up, in a hot 2 M NaOH solution for 30 min. Next, the PMMA/WSe₂ was washed by transferring them into DI water (4 times). Finally, the PMMA/WSe₂ was scooped out in pieces onto TEM grids and left under ambient conditions overnight to increase the adhesion between PMMA/WSe₂ and grid. PMMA was removed by vapor acetone. The grids were then annealed in vacuum chamber with high pressure ($\sim 10^{6}$ mbar) at 150 or 170 °C for at least 12 h before each TEM observation.

Conflict of Interest: The authors declare no competing financial interest.

Supporting Information Available: Experimental methods, supplementary text, Figures S1 to S18, Table 1 and 2, as mentioned in text, and references. This material is available free of charge *via* the Internet at http://pubs.acs.org.

REFERENCES AND NOTES

1. Kim, D. W.; Kim, Y. H.; Jeong, H. S.; Jung, H.-T. Direct Visualization of Large-Area Graphene Domains and Boundaries by Optical Birefringency. *Nat. Nanotechnol.* **2012**, *7*, 29–34.
2. Huang, P. Y.; Ruiz-Vargas, C. S.; van der Zande, A. M.; Whitney, W. S.; Levendorf, M. P.; Kevek, J. W.; Garg, S.; Alden, J. S.; Hustedt, C. J.; Zhu, Y.; *et al.* Grains and Grain Boundaries in Single-Layer Graphene Atomic Patchwork Quilts. *Nature* **2011**, *469*, 389–392.
3. Najmaei, S.; Liu, Z.; Zhou, W.; Zou, X.; Shi, G.; Lei, S.; Yakobson, B. I.; Idrobo, J.-C.; Ajayan, P. M.; Lou, J. Vapour Phase Growth and Grain Boundary Structure of Molybdenum Disulphide Atomic Layers. *Nat. Mater.* **2013**, *12*, 754–759.
4. Duong, D. L.; Han, G. H.; Lee, S. M.; Gunes, F.; Kim, E. S.; Kim, S. T.; Kim, H.; Ta, Q. H.; So, K. P.; Yoon, S. J.; *et al.* Probing Graphene Grain Boundaries with Optical Microscopy. *Nature* **2012**, *490*, 235–239.
5. Van der Zande, A. M.; Huang, P. Y.; Chenet, D. A.; Berkelbach, T. C.; You, Y.; Lee, G.-H.; Heinz, T. F.; Reichman, D. R.; Muller, D. A.; Hone, J. C. Grains and Grain Boundaries in Highly Crystalline Monolayer Molybdenum Disulphide. *Nat. Mater.* **2013**, *12*, 554–561.
6. Zhu, W. C.; Low, T.; Lee, Y.-H.; Wang, H.; Farmer, D. B.; Kong, J.; Xia, F.; Avouris, P. Electronic Transport and Device Prospects of Monolayer Molybdenum Disulphide Grown by Chemical Vapour Deposition. *Nat. Commun.* **2014**, *5*, 3087–3094.
7. Ghorbani-asl, M.; Enyashin, A. N.; Kuc, A.; Seifert, G.; Heine, T. Defect-Induced Conductivity Anisotropy in MoS₂ Monolayers. *Phys. Rev. B* **2013**, *88*, 245440.
8. Yuan, S.; Roldán, R.; Katsnelson, M. I.; Guinea, F. Effect of Point Defects on the Optical and Transport Properties of MoS₂ and WS₂. *Phys. Rev. B* **2014**, *90*, No. 041402.
9. Islam, M. R.; Kang, N.; Bhanu, U.; Paudel, H. P.; Erementchouk, M.; Terard, L.; Leuenberger, M. N.; Khondaker, S. I. Tuning the Electrical Property *via* Defect Engineering of Single Layer MoS₂ by Oxygen Plasma. *Nanoscale* **2014**, *6*, 10033–10039.

10. Yu, Q.; Jauregui, L. A.; Wu, W.; Colby, R.; Tian, J.; Su, Z.; Cao, H.; Liu, Z.; Pandey, D.; Wei, D.; *et al.* Control and Characterization of Individual Grains and Grain Boundaries in Graphene Grown by Chemical Vapour Deposition. *Nat. Mater.* **2011**, *10*, 443–449.

11. Ly, T. H.; Duong, D. L.; Ta, Q. H.; Yao, F.; Vu, Q. A.; Jeong, H. Y.; Chae, S. H.; Lee, Y. H. Nondestructive Characterization of Graphene Defects. *Adv. Funct. Mater.* **2013**, *23*, 5183–5189.

12. Son, J.-H.; Baeck, S.-J.; Park, M.-H.; Lee, J.-B.; Yang, C.-W.; Song, J.-K.; Zin, W.-C.; Ahn, J.-H. Detection of Graphene Domains and Defects Using Liquid Crystals. *Nat. Commun.* **2014**, *5*, 3484.

13. Enyashin, A. N.; Bar-Sadan, M.; Houben, L.; Seifert, G. Line Defects in Molybdenum Disulfide Layers. *J. Phys. Chem. C* **2013**, *117*, 10842–10848.

14. Zhou, W.; Zou, X.; Najmaei, S.; Liu, Z.; Shi, Y.; Kong, J.; Lou, J.; Ajayan, P. M.; Yakobson, B. I.; Idrobo, J.-C. Intrinsic Structural Defects in Monolayer Molybdenum Disulfide. *Nano Lett.* **2013**, *13*, 2615–2622.

15. Zhang, Y.; Zhang, Y.; Ji, Q.; Ju, J.; Yuan, H.; Shi, J.; Gao, T. Controlled Growth of High-Quality Monolayer WS_2 Layers on Sapphire. *ACS Nano* **2013**, *7*, 8963–8971.

16. Yin, X.; Ye, Z.; Chenet, D. A.; Ye, Y.; O'Brien, K.; Shi, J.; Hone, J. C. Edge Nonlinear Optics on a MoS_2 Atomic Monolayer. *Science* **2014**, *344*, 488–490.

17. Tongay, S.; Suh, J.; Ataca, C.; Fan, W.; Luce, A.; Kang, J. S.; Liu, J.; Ko, C.; Raghunathanan, R.; Zhou, J.; *et al.* Defects Activated Photoluminescence in Two-Dimensional Semiconductors: Interplay between Bound, Charged, and Free Excitons. *Sci. Rep.* **2013**, *3*, 2657.

18. Güneş, F.; Han, G. H.; Shin, H.-J.; Lee, S. Y.; Jin, M.; Duong, D. L.; Chae, S. J.; Kim, E. S.; Yao, F.; Benayad, A.; *et al.* UV-Light-Assisted Oxidative sp³ Hybridization of Graphene. *Nano* **2011**, *06*, 409–418.

19. Huang, J.-K.; Pu, J.; Hsu, C.-H.; Chiu, M.-H.; Juang, Z.-Y.; Chang, Y.-H.; Chang, W.-H.; Iwasa, Y.; Takenobu, T.; Li, L.-J. Large-Area Synthesis of Highly Crystalline WSe_2 Monolayers and Device Applications. *ACS Nano* **2014**, *8*, 923–930.

20. Lee, G.; Lee, B.; Kim, J.; Cho, K. Ozone Adsorption on Graphene: Ab *Initio* Study and Experimental Validation. *J. Phys. Chem. C* **2009**, *113*, 14225–14229.

21. Jandhyala, S.; Mordi, G.; Lee, B.; Lee, G.; Floresca, C.; Cha, P.-R.; Ahn, J.; Wallace, R. M.; Chabal, Y. J.; Kim, M. J.; *et al.* Atomic Layer Deposition of Dielectrics on Graphene Using Reversibly Physisorbed Ozone. *ACS Nano* **2012**, *6*, 2722–2730.

22. Feiyan, C.; Pehkonen, S. O.; Ray, M. B. Kinetics and Mechanisms of UV-Photodegradation of Chlorinated Organics in the Gas Phase. *Water Res.* **2002**, *36*, 4203–4214.

23. Wang, J. H.; Ray, M. B. Application of Ultraviolet Photooxidation to Remove Organic Pollutants in the Gas Phase. *Sep. Purif. Technol.* **2000**, *19*, 11–20.

24. Li, H.; Lu, G.; Wang, Y.; Yin, Z.; Cong, C.; He, Q.; Wang, L.; Ding, F.; Yu, T.; Zhang, H. Mechanical Exfoliation and Characterization of Single- and Few-Layer Nanosheets of WSe_2, TaS_2, and $TaSe_2$. *Small* **2013**, *9*, 1974–1981.

25. Sahin, H.; Tongay, S.; Horzum, S.; Fan, W.; Zhou, J.; Li, J.; Wu, J.; Peeters, F. Anomalous Raman Spectra and Tthickness-Dependent Electronic Properties of WSe_2. *Phys. Rev. B* **2013**, *87*, 165409.

26. Zeng, H.; Liu, G.-B.; Dai, J.; Yan, Y.; Zhu, B.; He, R.; Xie, L.; Xu, S.; Chen, X.; Yao, W.; *et al.* Optical Signature of Symmetry Variations and Spin-Valley Coupling in Atomically Thin Tungsten Dichalcogenides. *Sci. Rep.* **2013**, *3*, 1608.

27. Jiang, H. Electronic Band Structures of Molybdenum and Tungsten Dichalcogenides by the GW Approach. *J. Phys. Chem. C* **2012**, *116*, 7664–7671.

28. Li, H.; Wu, J.; Yin, Z.; Zhang, H. Preparation and Applications of Mechanically Exfoliated Single-Layer and Multilayer MoS_2 and WSe_2 Nanosheets. *Acc. Chem. Res.* **2014**, *47*, 1067–1075.

29. Mouri, S.; Miyauchi, Y.; Matsuda, K. Tunable Photoluminescence of Monolayer MoS_2 *via* Chemical Doping. *Nano Lett.* **2013**, *13*, 5944–5948.

30. Kumar, A.; Ahluwalia, P. K. Electronic Structure of Transition Metal Dichalcogenides Monolayers 1H-MX2 (M = Mo, W; X = S, Se, Te) from *ab Initio* Theory: New Direct Band Gap Semiconductors. *Eur. Phys. J. B* **2012**, *85*, 186.

31. Lehtinen, O.; Kaiser, U.; Krasheninnikov, A. V. Two-Dimensional Transition Metal Dichalcogenides under Electron Irradiation: Defect Production and Doping. *Phys. Rev. Lett.* **2012**, *109*, 035503.

32. Algara-siller, G.; Kurasch, S.; Sedighi, M.; Lehtinen, O.; Kaiser, U. The Pristine Atomic Structure of MoS_2 Monolayer Protected from Electron Radiation Damage by Graphene. *Appl. Phys. Lett.* **2013**, *103*, 203107.

33. Komsa, H.-P.; Kurasch, S.; Lehtinen, O.; Kaiser, U.; Krasheninnikov, A. V. From Point to Extended Defects in Two-Dimensional MoS_2: Evolution of Atomic Structure under Electron Irradiation. *Phys. Rev. B* **2013**, *88*, 035301.